



## **Magnetocardiography on an isolated animal heart with a room-temperature optically pumped magnetometer**

Jensen, Kasper; Skarsfeldt, Mark Alexander; Staerkind, Hans; Arnbak, Jens; Balabas, Mikhail V.; Olesen, Soren-Peter; Bentzen, Bo Hjorth; Polzik, Eugene S.

*Published in:*  
Scientific Reports

*DOI:*  
[10.1038/s41598-018-34535-z](https://doi.org/10.1038/s41598-018-34535-z)

*Publication date:*  
2018

*Document version*  
Publisher's PDF, also known as Version of record

*Document license:*  
[CC BY](#)

*Citation for published version (APA):*  
Jensen, K., Skarsfeldt, M. A., Staerkind, H., Arnbak, J., Balabas, M. V., Olesen, S-P., Bentzen, B. H., & Polzik, E. S. (2018). Magnetocardiography on an isolated animal heart with a room-temperature optically pumped magnetometer. *Scientific Reports*, 8, [16218]. <https://doi.org/10.1038/s41598-018-34535-z>

# SCIENTIFIC REPORTS

OPEN

## Magnetocardiography on an isolated animal heart with a room-temperature optically pumped magnetometer

Kasper Jensen<sup>1,4</sup>, Mark Alexander Skarsfeldt<sup>2</sup>, Hans Stærkind<sup>1</sup>, Jens Arnbak<sup>1</sup>, Mikhail V. Balabas<sup>1,3</sup>, Søren-Peter Olesen<sup>2</sup>, Bo Hjorth Bentzen<sup>2</sup> & Eugene S. Polzik<sup>1</sup>

Optically pumped magnetometers are becoming a promising alternative to cryogenically-cooled superconducting magnetometers for detecting and imaging biomagnetic fields. Magnetic field detection is a completely non-invasive method, which allows one to study the function of excitable human organs with a sensor placed outside the human body. For instance, magnetometers can be used to detect brain activity or to study the activity of the heart. We have developed a highly sensitive miniature optically pumped magnetometer based on cesium atomic vapor kept in a paraffin-coated glass container. The magnetometer is optimized for detection of biological signals and has high temporal and spatial resolution. It is operated at room- or human body temperature and can be placed in contact with or at a mm-distance from a biological object. With this magnetometer, we detected the heartbeat of an isolated guinea-pig heart, which is an animal widely used in biomedical studies. In our recordings of the magnetocardiogram, we can detect the P-wave, QRS-complex and T-wave associated with the cardiac cycle in real time. We also demonstrate that our device is capable of measuring the cardiac electrographic intervals, such as the RR- and QT-interval, and detecting drug-induced prolongation of the QT-interval, which is important for medical diagnostics.

The cardiac function is based on conduction of electrical signals, which activate the heart muscle so that blood can be pumped throughout the body. Electrodes placed on the body surface can record this cardiac electrical activity. This method is called electrocardiography (ECG) and is commonly used for diagnosing heart diseases. The electrical signals propagating through the heart generate magnetic fields, which can be detected and imaged with sensitive magnetometers placed outside the body. This method called magnetocardiography (MCG) can be advantageous to use in certain cases including for measurements of the electrical activity in the fetal heart<sup>1</sup>. Detection of the magnetic field from the heart was first done using pick-up coils<sup>2</sup> and later with a superconducting quantum interference device (SQUID) magnetometer, which together with the development of a shielded room has led to improved signal-to-noise ratio of the observed magnetocardiograms<sup>3</sup>. SQUID magnetometers are highly sensitive but have a major drawback which is the requirement for cryogenic cooling. Optically pumped magnetometers (OPMs) can achieve similar high sensitivity but they do not require cryogenics and are considered promising for many applications, in particular for detecting brain activity<sup>4–6</sup> (magnetoencephalography) and for magnetocardiography on the adult<sup>7,8</sup> and fetal heart<sup>9–11</sup>. OPMs based on absorption of light and operating in the so-called spin-exchange relaxation-free (SERF) regime<sup>12</sup> are now commercially available<sup>13</sup>. SERF magnetometers have some disadvantages including an operating temperature of several hundreds of degrees Celsius, which leads to the need for thermal insulation. Also, SERF magnetometers should be operated in zero magnetic field and have a limited operational bandwidth (from DC up to typically 100 Hz) which is suitable for MCG but not for detection of signals with higher frequency components. Our OPM is based on cesium atomic vapor contained in

<sup>1</sup>Niels Bohr Institute, University of Copenhagen, Blegdamsvej 17, 2100, Copenhagen, Denmark. <sup>2</sup>Department of Biomedical Sciences, Faculty of Health and Medical Sciences, University of Copenhagen, Blegdamsvej 3, 2200, Copenhagen N, Denmark. <sup>3</sup>Department of Physics, St Petersburg State University, Universitetskii pr. 28, 198504, Staryi Peterhof, Russia. <sup>4</sup>Present address: School of Physics and Astronomy, University of Nottingham, University Park, Nottingham NG7 2RD, England, United Kingdom. Correspondence and requests for materials should be addressed to K.J. (email: [kjensen@nbi.dk](mailto:kjensen@nbi.dk))

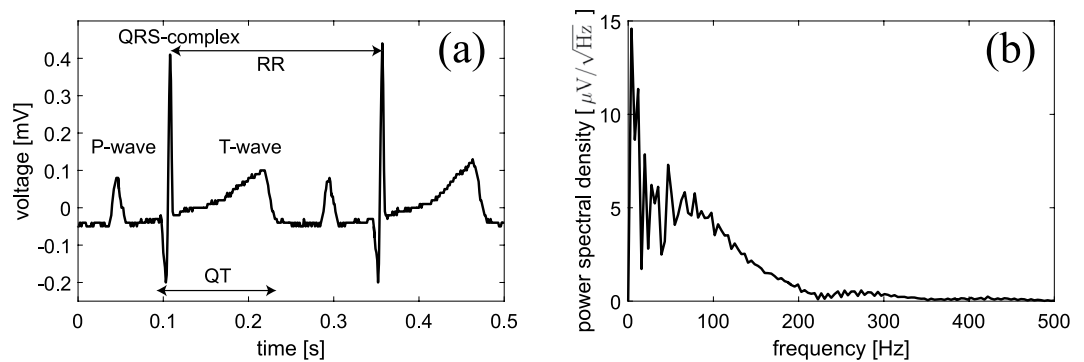


**Figure 1.** Electrical recording on an isolated guinea-pig heart placed in a Langendorff setup. **(a)** Electrocardiogram showing the P-wave, the QRS-complex and the T-wave. Electrographic intervals RR and QT are depicted with arrows. **(b)** Power spectral density of the electrocardiogram of a single heartbeat lasting approximately 0.25 s (RR = 247 ms corresponding to 243 bpm).

spin protecting environment and is operated at room- or human body temperature. This allows the magnetometer to be placed in contact with or at a mm-distance from biological tissue. Our type of cesium magnetometer is versatile and can be used to detect time-varying signals with frequency components ranging from DC to MHz and it can have a large and tunable bandwidth (see Methods). For instance, this type of magnetometer was used for detecting radio-frequency magnetic fields with sub-fT/ $\sqrt{\text{Hz}}$  sensitivity<sup>14</sup>. More recently, the magnetometer was employed in biomedical experiments where it was used to detect action potentials from an isolated animal nerve<sup>15</sup>. There the magnetometer was tuned (by adjusting the bias magnetic field) to have maximum response at around 500 Hz as the action potentials had the largest frequency components around that frequency. In the present work, the magnetometer is operated at close to zero field (just as SERF magnetometers are) and has a maximum response at DC as this is optimal for detection of the MCG. Note also that recently MCG from an adult person was detected with a room-temperature OPM based on  $^4\text{He}$ <sup>16</sup>.

Early diagnosis and intervention on cardiac conduction abnormalities before birth can be lifesaving. Although the development and improvement of echocardiography<sup>17</sup> has been instrumental in managing fetal arrhythmia, it is limited as it measures the mechanical consequence of the arrhythmia rather than the electrical activity underlying the arrhythmia. Fetal MCG with detection of the cardiac electrical activity can help to understand the electrical mechanism underlying fetal arrhythmias<sup>18</sup> such as, bradycardia, atrio-ventricular block<sup>19</sup> and supraventricular tachycardia<sup>20</sup> and hence guide correct treatment. Another example of this is the fetal diagnosis of long QT syndrome (LQTS)<sup>21,22</sup>. Congenital LQTS is a heritable arrhythmia syndrome, with a prevalence of 1:2500 in healthy live births<sup>23</sup>, characterized by delayed repolarization of the ventricular cardiac action potential, which manifests itself as a prolonged QT-interval on the ECG. It is most often caused by mutations in genes responsible for the repolarization of the ventricular cardiac action potential, and results in an increased risk of ventricular arrhythmia, and consequently is an important contributor to sudden cardiac death in newborns and young<sup>24</sup>. Detection of LQTS in fetuses is important in order to decrease fetal morbidity<sup>25</sup>. However, because fetal ECG recordings are currently not feasible and echocardiography cannot be used to detect prolonged QT-intervals, there is a need for novel non-invasive tools for prenatal LQTS detection. Non-invasive magnetocardiography would enable healthcare professionals to diagnose these abnormalities. Using the guinea pig heart that has comparable size (see Methods section), heart rate<sup>26,27</sup> and electrical properties<sup>28</sup> to that of a heart from a human fetus at gestational age of 18–22 weeks, we demonstrate that our magnetometer is capable of detecting the cardiogram in real-time and capable of detecting changes in the QT interval of the cardiogram. This shows that OPMs are promising devices for biomedical studies and for diagnosis of fetal heart diseases.

## Results

**Guinea-pig electrocardiogram.** In this study we perform experiments on isolated guinea-pig hearts having about the same size as a human fetus heart. A detailed description of the heart preparation is provided in the Methods section. Before any magnetic field measurements are initiated, the electrically active, spontaneously beating heart being perfused with physiological solution is first placed in a separate Langendorff setup<sup>29</sup>. An example of an ECG measured in the Langendorff setup is shown in Fig. 1(a). The P-wave, QRS-complex and the T-wave are all clearly visible. A single heartbeat [corresponding to the time-interval from 0 to 0.25 s in Fig. 1(a)] has frequency components mainly in the range from DC–200 Hz as seen in Fig. 1(b). As discussed in detail below, our magnetometer is capable of detecting such signals with high sensitivity.

**Experimental setup.** Our magnetometer is based on cesium atomic vapor kept in a paraffin-coated miniature glass container [see Fig. 2(a)] with inner size 5 mm × 5 mm × 5 mm and 0.7 mm glass-wall thickness. The vapor cell is kept at room- or human body temperature and is placed inside a multi-layer cylindrical magnetic shield. Circularly polarized pump (wavelength  $\approx 895$  nm) and repump (wavelength  $\approx 852$  nm) laser light on resonance with the cesium D1 and D2 transitions, respectively, is used for optical pumping [Fig. 2(b,c)]. Linearly polarized laser light (wavelength  $\approx 852$  nm) near-resonant with the cesium D2 transition ( $\approx 1600$  GHz detuning)

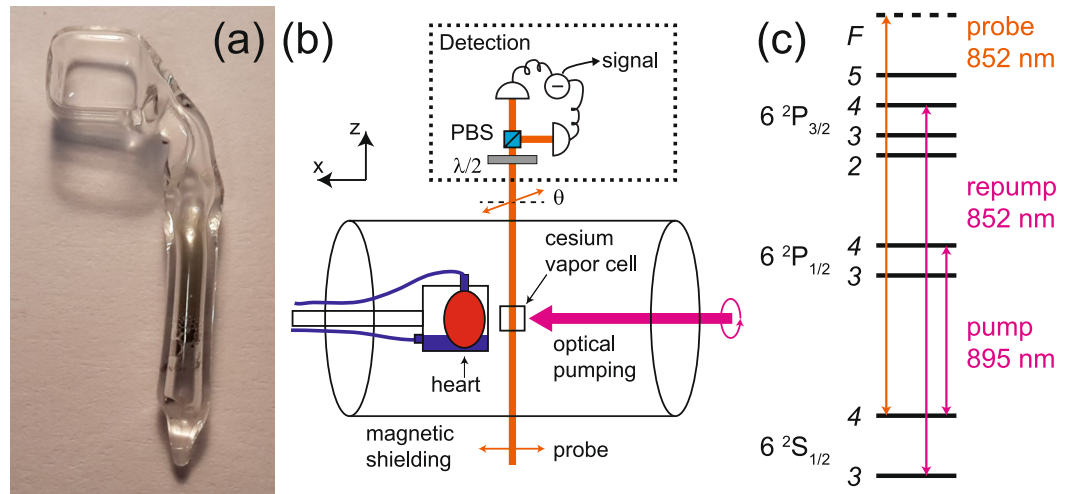


**Figure 2.** Experimental setup. (a) Picture of the cesium vapor cell. (b) Schematic of the experimental setup. λ/2: half-wave plate, PBS: polarizing beamsplitter. The magnetic field from the heart affects the cesium atomic spins which in turn rotates the polarization of the probe light by an angle  $\theta$ . This polarization rotation is detected with a balanced polarimeter (shown inside the dashed-line box). (c) Cesium atom level scheme and laser frequencies.

is used to probe the spin-polarized cesium atoms. Any magnetic field will affect the atomic spins which in turn will lead to a rotation of the probe light polarization. This rotation is detected with a balanced detection scheme [see Fig. 2(c)] which gives a magnetometer signal from which we can infer the magnetic field (see details below).

**Model of the magnetometer.** The cesium atoms are described by their total angular momentum  $\mathbf{J} = (J_x, J_y, J_z)$  which in the absence of any magnetic field is optically pumped along the x-direction using circular polarized light. A fully spin-polarized ensemble of cesium atoms corresponds to the spin vector  $\mathbf{J}_{\text{max}} = (4N_A, 0, 0)$  for  $N_A$  atoms in the  $F = 4, m_x = 4$  ground state hyperfine sublevel. In a simplified model of the magnetometer, the time-evolution of the spin vector can be described by the following differential equation<sup>30</sup>

$$\frac{d\mathbf{J}}{dt} = \gamma \mathbf{J} \times \mathbf{B} + \Gamma_p \mathbf{J}_{\text{max}} - (\Gamma_p + \Gamma_{\text{pr}} + \Gamma_{\text{dark}}) \mathbf{J}, \quad (1)$$

where  $\mathbf{B}$  is the external magnetic field and  $\gamma = 2.2 \cdot 10^{10} \text{ rad}/(\text{s} \cdot \text{T})$  is the cesium gyromagnetic ratio. In the above, optical pumping happens with a rate  $\Gamma_p$  and the spin decays with a total rate  $\Gamma = \Gamma_p + \Gamma_{\text{pr}} + \Gamma_{\text{dark}}$ , where  $\Gamma_{\text{pr}}$  is the probe-induced decay rate and  $\Gamma_{\text{dark}}$  is the decay rate in the absence of any light.  $\Gamma_p$  and  $\Gamma_{\text{pr}}$  are proportional to the power of the pump and probe laser light, respectively. The atomic spin and thereby the magnetic field is detected by sending a near-resonant and linearly-polarized probe laser beam through the atoms and recording the light polarization rotation which is proportional to the spin-component  $J_z$  along the probe direction<sup>15</sup>.

If we assume that the magnetic field is static or varying slowly on the time-scale set by  $T_2 = 1/\Gamma$ , we can solve Eq. (1) in the steady-state, and if we furthermore assume that the magnetic field is small  $|B|^2 \ll \Delta B^2$ , where  $\Delta B = \Gamma/\gamma$ , we find that the magnetometer signal  $S(t) \propto J_z(t) = J_0 B_y(t)/\Delta B$ , where  $J_0 = J_{\text{max}} \Gamma_p/\Gamma$  (see Methods section). I.e., the magnetometer signal is proportional to the y-component of the magnetic field. On the other hand, if the field is varying on a time-scale comparable to  $T_2$  or faster, we find that the magnetometer signal is

$$S(t) = c \int_{t'=-\infty}^{t'=t} e^{-\Gamma(t-t')} B_y(t') dt', \quad (2)$$

where  $c$  is a normalization constant and we again assumed that the magnetic field is small (see Methods section). In this case, the magnetometer signal is a convolution of the y-component of the magnetic field with the magnetometer response function  $c \cdot e^{-\Gamma t}$ . The magnetic field  $B_y(t)$  can then be obtained by deconvolving the magnetometer signal  $S(t)$  with the response function.

**Calibrating the magnetometer.** The magnetometer is calibrated before any biomagnetic measurements. Even though the magnetometer is placed inside a magnetic shield, there will be a small residual static field. Three sets of coils are used to apply magnetic fields along the x-, y-, and z-directions in order to cancel the residual field such that the total field is approximately zero. In order to measure the temporal profile  $e^{-\Gamma t}$  of the magnetometer response function, an extra coil is used to apply a short square pulse (100 μs duration) of magnetic field along the y-direction. The observed magnetometer signal [solid line in Fig. 3(a)] increases rapidly and then decays exponentially with time-constant  $T_2 = 4.0 \text{ ms}$  and is in good agreement with the model given by Eq. (1). Notice that due to power broadening by the probe, pump and repump light, the decay-time is significantly shorter than the coherence time in the dark  $T_2^{\text{dark}} = 1/\Gamma_{\text{dark}} > 50 \text{ ms}$ . For our type of vapor cell, a long  $T_2^{\text{dark}}$  is possible due to the

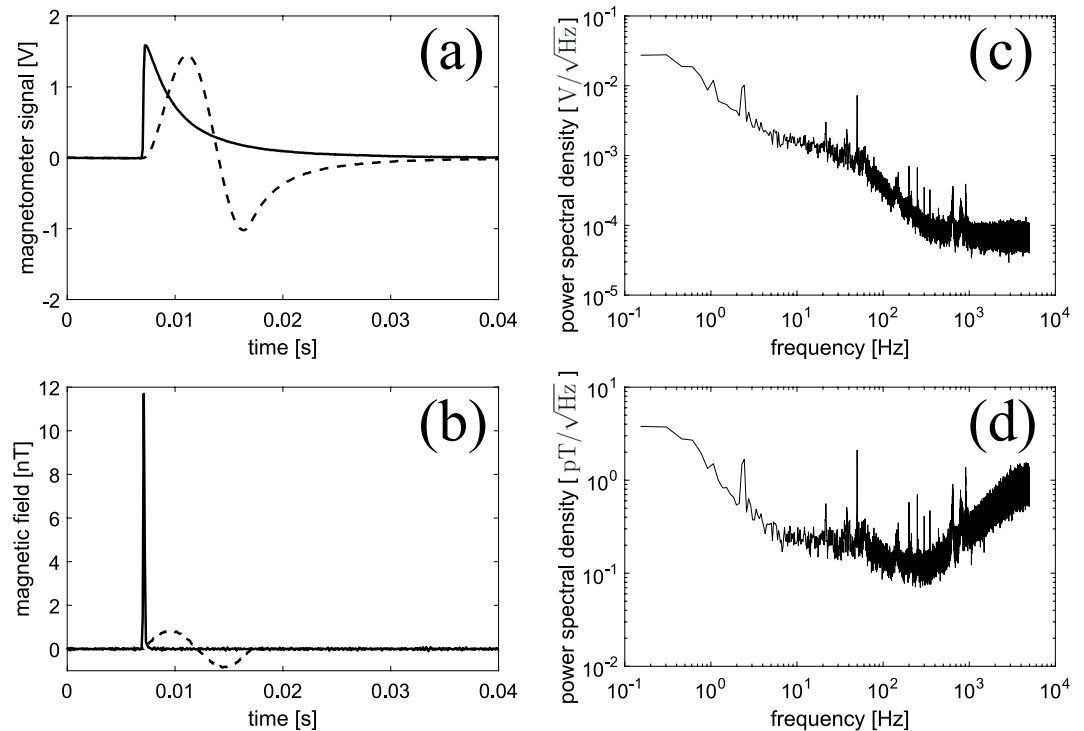


**Figure 3.** Magnetic field measurements. (a) Magnetometer signal in volts. Solid line: 100  $\mu$ s square magnetic pulse applied. Dashed line: single sine wave magnetic pulse with 10 ms period applied. Signals have been averaged 10 times. (b) Magnetic field in nT as calculated by deconvolving the signals in (a). (c) Magnetometer noise spectrum in  $V/\sqrt{\text{Hz}}$  (without any applied magnetic field). Noise spectrum has been averaged 10 times. (d) Noise spectrum in  $\text{pT}/\sqrt{\text{Hz}}$ . The temperature  $\approx 26^\circ\text{C}$  of the cesium vapor cell was slightly above room temperature.

paraffin-coating inside the vapor cell which preserves the spin of the moving cesium atoms during collisions with the glass walls.

We then apply a magnetic field pulse with the temporal shape of a single sinusoidal oscillation with 10 ms period and independently calibrated amplitude. By numerically deconvolving the measured signal [dashed line in Fig. 3(a)] with the un-normalized response function  $e^{-T}$  and comparing the amplitude of the deconvoluted signal with the independently calibrated amplitude, we can extract the normalization constant  $c$ , and calculate the magnetic fields in nT or pT as shown Fig. 3(b).

We also record the magnetometer background noise when there is no magnetic field pulse applied. The corresponding noise spectrum is shown in Fig. 3(c). At frequencies above 1 kHz the noise is white, i.e. independent of frequency, and is mainly due to the shot noise of the probe light. At lower frequencies the noise level is higher (see Discussion section). The noise spectrum in magnetic field units found by deconvolution is shown in Fig. 3(d). We achieve the best sensitivity of around 120  $\text{fT}/\sqrt{\text{Hz}}$  for frequencies in the 100–500 Hz range, and around or better than 300  $\text{fT}/\sqrt{\text{Hz}}$  for frequencies in the wider range 5–1000 Hz.

We note that the atomic bandwidth  $1/(2\pi T_2)$  can be widely tuned by adjusting the power of the probe and/or pump lasers. For our specific settings, the atomic bandwidth is 40 Hz. The advantage of the deconvolution procedure is that it allows one to correctly find the temporal profile of magnetic fields with much higher frequency components up to the one half times the data-acquisition sample-rate which in our case is  $\frac{1}{2} \times 10 \text{ kHz} = 5 \text{ kHz}$ . The magnetic field from the heart is expected to have frequency components in the DC–200 Hz range which is outside the atomic bandwidth. The deconvolution procedure is therefore necessary in order to correctly find the temporal profile of a magnetocardiogram, and in particular for finding the correct amplitudes of the QRS-complex and the P-wave which are the fastest-varying features of the cardiogram. The deconvolution procedure also amplifies high frequency noise, and in case the signal is small, additional low-pass or bandpass filtering may be required in order to obtain a sufficient signal-to-noise ratio. When recording the magnetic field from the heart, we choose to low-pass filter the deconvoluted signals using a Type I Chebyshev filter with a cut-off frequency of either 250 Hz or 500 Hz. A cut-off frequency of 250 Hz or 500 Hz is high enough such that one can correctly capture the temporal profiles and amplitudes of the QRS-complex and P-wave and low enough to suppress high-frequency noise and thereby improve the signal-to-noise ratio.

**Magnetic field from the isolated guinea-pig heart.** During the biomagnetic measurements, the spontaneously beating guinea-pig heart is put in a watertight acrylic container [see Fig. 4(a)] and placed close to the vapor cell. The position of the heart relative to the vapor cell can be set using a three-axis translation stage with travel range of 25 mm. The smallest possible distance between the heart and the center of the vapor cell is 5.2 mm

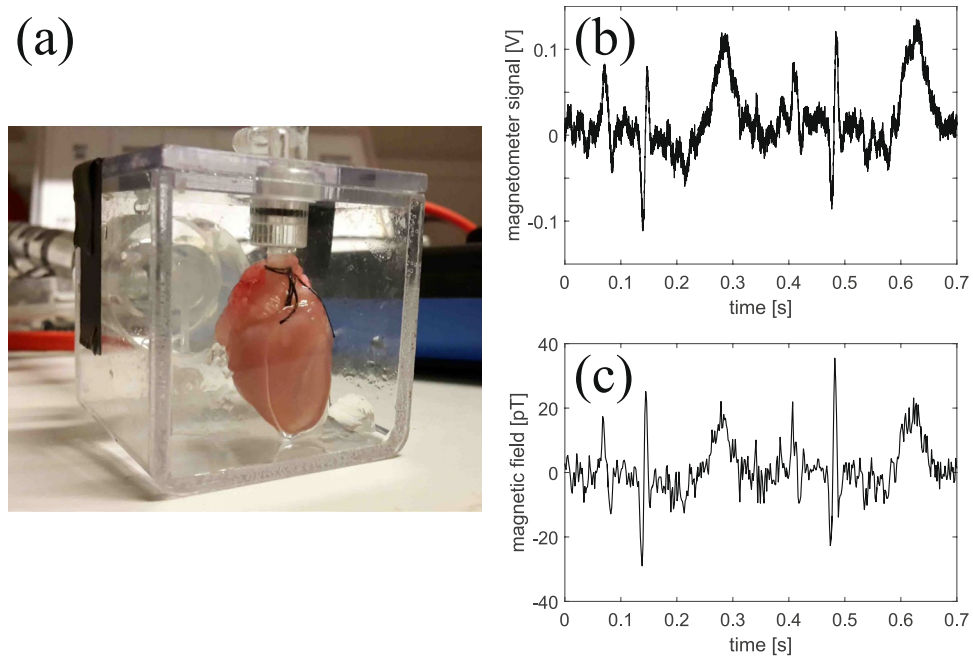


**Figure 4.** Guinea-pig heart and the magnetocardiogram. **(a)** Picture of an isolated guinea-pig heart inside a plastic chamber. **(b)** Example of a magnetometer signal (without averaging) in volts when a guinea-pig heart is placed close to the magnetometer. **(c)** Magnetic field from the heart in pT. The deconvoluted signal was low-pass filtered using a Type I Chebyshev filter with a cut-off frequency of 250 Hz to suppress high-frequency noise. The temperature  $\approx 26^\circ\text{C}$  of the cesium vapor cell was slightly above room temperature due to heating from the heart which was perfused with  $\approx 37^\circ\text{C}$  warm physiological solution.

(2 mm thickness of acrylic container, 2.5 mm inside radius of vapor cell and 0.7 mm glass-wall thickness). Our magnetometer measures the  $y$ -component of the magnetic field (see Fig. 2c) which is a component of the field parallel to the surface of the heart.

An example of a real-time recording of the magnetometer signal is shown in Fig. 4(b). We note that it is possible to see the P-wave, QRS-complex and T-wave in real-time without the use of averaging. The magnetic field found by deconvolution is shown in Fig. 4(c). The QRS complex has duration  $\approx 25$  ms and is varying on a time-scale comparable to  $T_2$ . The deconvolution procedure is therefore necessary to correctly find the QRS amplitude which for this particular magnetocardiogram is approximately 55 pT peak-to-peak.

The actual shape or morphology of the magnetocardiogram depends on the position of the heart relative to the magnetometer. To illustrate this, we measured MCGs at  $4 \times 4 = 16$  different relative positions covering a  $15\text{ mm} \times 15\text{ mm}$  area close to the heart (see Supplementary Figure S1). The relative position was changed by translating the plastic chamber containing the heart in the  $y$ - $z$ -plane (see Fig. 2c) in steps of 5 mm. In Supplementary Figure S2, we clearly see that the temporal shape of the magnetocardiograms depend on the position. This is even more apparent in the zoom-ins of the QRS-complexes shown in Supplementary Figure S3. For instance, it seems like the magnetic field changes direction/sign depending on whether the magnetometer is in front of the right or left side of the heart. Also the amplitude of the QRS-complex depends on position. In those measurement, the peak-to-peak amplitude varied in the range 50–120 pT. We note that because we only use a single magnetic field sensor, and not a whole magnetometer array, measurements at different positions are recorded at different times. This is a problem if the heart is not beating at the same frequency over the whole scan period, something which is challenging to achieve because the heart is isolated from the guinea-pig, spontaneously beating and is sensitive to temperature and flow/pressure fluctuations of the Krebs-Henseleit buffer (see Methods section) used to perfuse the heart. Despite such possible issues, our magnetometer can indeed be placed close to the heart and be used to measure the magnetic field around the heart with high spatial resolution and good signal-to-noise ratio. The spatial resolution of the magnetometer is here defined to be 5 mm, as the magnetometer measures the average magnetic field inside the  $(5\text{ mm})^3$  volume of the vapor cell.

For one of the positions in the  $y$ - $z$ -plane, we also varied the distance between the heart and the magnetometer from 6–16 mm (along the  $x$ -direction, see Fig. 2c). In those measurements, the QRS amplitude dropped from  $\approx 100$  pT peak-to-peak to less than 15 pT peak-to-peak as seen in Fig. 5. The QRS amplitude as a function of distance was fitted to a function  $B_{\text{pp}}^{\text{QRS}} \propto x^{-n}$ , where the fitted value  $n = 1.7(2)$  was obtained. The fit can be used to estimate the signal at larger distances relevant for fetal magnetocardiography. For instance, for  $x = 50$  mm, the extrapolation of the fitted curve gives  $B_{\text{pp}}^{\text{QRS}}(50\text{ mm}) = 2.4\text{ pT}$  which is  $\approx 40$  times smaller than the field at  $x = 6$  mm.

The magnetic field close to the heart varies significantly on the 5 mm length scale (see Figs 5 and S2 and S3). For detection of the field close to the heart, it may therefore be an advantage to use a magnetometer with a smaller sensing volume. Note however that the sensitivity of an optically pumped magnetometer depends on the sensing



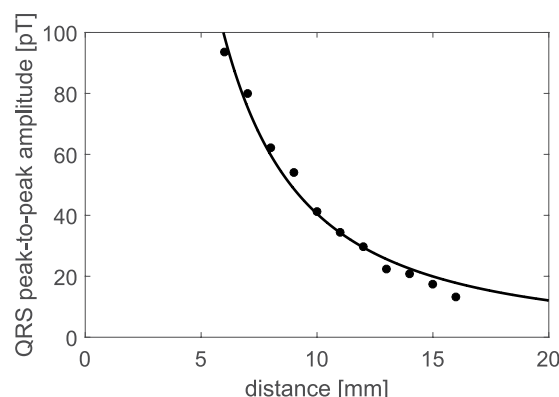


**Figure 5.** Peak-to-peak value of the QRS complex as a function of distance between the heart and magnetometer.

volume (see Methods) and that a smaller magnetometer would have worse sensitivity. For future measurements of the fetal heartbeat which will be performed at  $\geq 5$  cm sensor-heart distance, a larger vapor cell may be optimal.

**Drug-induced prolongation of the QT interval.** We pharmacologically mimicked inherited LQTS using a potent ion channel blocker (E-4031), that in sub-micro molar concentrations blocks the rapid delayed rectifying repolarizing current ( $I_{Kr}$ ), and results in prolongation of the QT-interval (see Methods section). Before the measurements, the isolated hearts were allowed to stabilize in the watertight container for approximately 30 minutes. Then, a baseline measurement of the MCG was performed before adding QT-prolonging drug (E-4031) to the perfusion fluid. The effect of the QT-prolonging drug is not instantaneous so for that reason we measured MCGs every 5th minute for a 20-minute time frame [see example MCGs in Fig. 6(a)] to ascertain the full effect was achieved. Throughout the experiment, the coronary artery flow was kept constant by adjusting the perfusion pressure in order to ensure a stable physiological temperature of the heart. We repeated the experiment using in total five isolated guinea-pig hearts. As seen in Fig. 6(b,c), we are able to detect the QT-prolongation of  $0.06 \mu\text{M}$  E-4031 and detect a decrease in heart rate using our optically pumped magnetometer.

## Discussion

In conclusion, we have demonstrated that our optically pumped magnetometer can be used for real-time monitoring of the heartbeat of an isolated guinea-pig heart. We have furthermore imaged the magnetic field around the heart, measured how the field decays with distance, and showed that the magnetometer can be used in biomedical studies and to diagnose cardiac repolarization abnormalities such as LQTS. The measurements are possible due to the high sensitivity of the magnetometer and its operating temperature and small size which make it possible to place the magnetometer in contact with or at just a few mm distance from a biological object. The current sensitivity of the magnetometer is around  $120\text{--}300 \text{ fT}/\sqrt{\text{Hz}}$  for a wide frequency range  $5\text{--}1000 \text{ Hz}$ . The sensitivity is ultimately limited by the quantum spin-projection noise of the cesium atoms which is estimated to be  $4 \text{ fT}/\sqrt{\text{Hz}}$  (see discussion of the sensitivity in the Methods section). Achieving this sensitivity would lead to an improved signal-to-noise ratio of a factor  $30\text{--}75$  which would make the quality of the recorded MCGs outstanding. Such an improved sensitivity would also allow for real-time recordings of MCGs at larger distances. Based on our measurements on the guinea-pig heart, we conclude that real-time detection of the heartbeat of a human fetus at gestational age of  $18\text{--}22$  weeks, where the heart-sensor distance is estimated to be  $\geq 5$  cm, should be possible. We also note, that our OPM works at physiological temperatures, which would allow for probes designed for use inside the human body. The advantage with that approach is that signals would be much larger when the sensor is close to the object under investigation.

Further development of an array of OPMs<sup>31,32</sup> operating at physiological temperature would be beneficial as this would allow for fast and simultaneous recording of the field at many positions. This would enable 3D-reconstruction of the distribution of ionic currents flowing inside the heart, similar to what is done in neuroscience when a SQUID magnetometer array is used to image brain activity. Note however, that the cardiac intervals such as RR and QT do not depend on the position of the magnetometer with respect to the heart. This means that for diagnosing elevated heart rate or QT-prolongation, only a single sensor is required. In fetal-magnetocardiography, using a few sensors will be beneficial: one sensor would record the fetal-MCG, another sensor the mother's MCG, and a few other sensors would monitor and correct for drifts in the background field. An array of OPMs working at physiological temperatures may also be interesting for biomedical or pre-clinical studies. It would allow for monitoring the propagation of action potentials with high spatial resolution in for instance isolated nerves<sup>15</sup> or brain tissue. The combination of an OPM array and a guinea-pig heart could also be interesting for imaging and studying the local electrical conductivity of the heart<sup>33</sup>. In conclusion, we believe that OPMs are promising devices for biomedical and pre-clinical studies, and that OPMs will have clinical use as a new diagnostic tool that will allow clinicians to do better diagnostics and prenatal care.

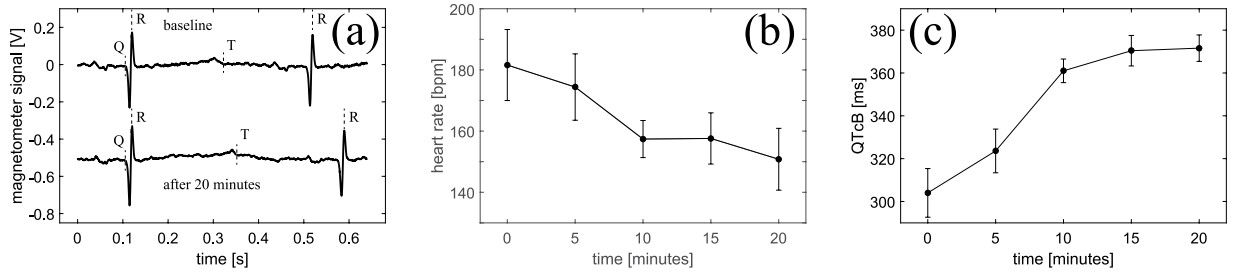


**Figure 6.** Effects of  $I_{K_r}$  inhibition on heart rate and QT-interval. **(a)** Example magnetometer signals recorded before and after administration of  $0.06 \mu\text{M}$  E-4031. Traces are the averages of approximately 10 heartbeats. **(b)** Heart rate in beats per minute:  $\text{bpm} = 60/\text{RR-interval [s]}$ . Points are mean values averaged over 5 animals. Error bars represent the standard error of the mean. **(c)** QT-interval corrected for heart rate (Bazett correction<sup>35</sup>). In **(b)** and **(c)**, heart rate and QT-intervals are measured before ( $t=0$  data points) and 5, 10, 15, and 20 minutes after administration of the drug.

## Methods

**Evolution of the spin vector in a magnetic field.** The evolution of the cesium atomic spins in an external magnetic field is modeled using Eq. (1). If we assume that the magnetic field is static or varying slowly on the time-scale set by  $1/\Gamma$ , we can solve the equation in the steady-state and find the solution

$$J_x^{ss} = J_0 \frac{B_x^2 + (\Delta B)^2}{|B|^2 + (\Delta B)^2}, \quad (3)$$

$$J_y^{ss} = J_0 \frac{B_x B_y - B_z \Delta B}{|B|^2 + (\Delta B)^2}, \quad (4)$$

$$J_z^{ss} = J_0 \frac{B_x B_z + B_y \Delta B}{|B|^2 + (\Delta B)^2}, \quad (5)$$

where  $|B|^2 = B_x^2 + B_y^2 + B_z^2$ ,  $\Delta B = \Gamma/\gamma$  and  $J_0 = J_{\max} \Gamma_p/\Gamma$ . If we furthermore assume that the magnetic field is small  $|B|^2 \ll \Delta B^2$ , we find the steady state spin vector  $\mathbf{J}^{ss} \approx J_0(1, -B_z/\Delta B, B_y/\Delta B)$ .

We can also solve Eq. (1) for the case where the magnetic field is varying on a time-scale comparable to  $1/\Gamma$  or faster. We will assume that the field can be written as  $\mathbf{B}(t) = B_0 \hat{x} + \delta \mathbf{B}(t)$ , where  $B_0$  is a static field pointing in the  $x$ -direction and  $\delta \mathbf{B}(t) = (\delta B_x(t), \delta B_y(t), \delta B_z(t))$  is a small time-varying magnetic field which can be treated as a perturbation. To first order in  $\delta \mathbf{B}(t)$ , we find the magnetometer signal

$$S(t) \propto J_z(t) = \gamma J_0 \int_{t'=-\infty}^{t'=t} e^{-\Gamma(t-t')} \{ \cos[2\pi\nu_L(t-t')] \delta B_y(t') - \sin[2\pi\nu_L(t-t')] \delta B_z(t') \} dt', \quad (6)$$

where  $\nu_L = \gamma B_0/(2\pi)$  is the Larmor frequency in Hz. We see that the magnetometer signal is a convolution of  $\delta B_y(t)$  with the magnetometer response function  $e^{-\Gamma t} \cos[2\pi\nu_L t]$  plus the convolution of  $\delta B_z(t)$  with the response function  $e^{-\Gamma t} \sin[2\pi\nu_L t]$ . Therefore, the magnetometer will mainly be sensitive to magnetic fields which are transverse to the static field and which have frequency components that are within a certain bandwidth set by  $\Gamma$  around the Larmor frequency  $\nu_L$ . Both  $\nu_L$  and  $\Gamma$  are widely tunable such that the magnetometer can be optimized for detection of specific time-varying magnetic fields. In our previous work we used non-zero static  $B_0$ -fields for detection of radio-frequency magnetic fields<sup>14</sup> and magnetic fields from animal nerve impulses<sup>15</sup>. Here, we instead choose a static field close to zero as the heartbeat has frequency components mainly in the range from DC-200 Hz. For  $B_0 = 0$ , Eq. (6) simplifies to the expression

$$S(t) \propto J_z(t) = \gamma J_0 \int_{t'=-\infty}^{t'=t} e^{-\Gamma(t-t')} \delta B_y(t') dt'. \quad (7)$$

We see that for  $B_0 = 0$ , the magnetometer is only sensitive to the  $y$ -component of the magnetic field, as opposed to the case  $B_0 \neq 0$  where the magnetometer is sensitive to both the  $y$ - and  $z$ -components of the field.

It is also instructive to calculate the response of the atomic system to a small oscillating magnetic field along the  $y$ -direction. If  $\mathbf{B}(t) = (0, B_{AC} \cos \omega t, 0)$ , then we find the signal

$$S(t) \propto J_z(t) = \gamma J_0 B_{AC} \frac{\Gamma \cos(\omega t) + \omega \sin(\omega t)}{\omega^2 + \Gamma^2} = \gamma J_0 B_{AC} \frac{\cos(\omega t - \phi)}{\sqrt{\omega^2 + \Gamma^2}}, \quad (8)$$



where  $\tan\phi = \omega/\Gamma$ . We see that the signal has components both in-phase (the term oscillating as a cosine) and out-of-phase (the term oscillating as a sine) with the applied magnetic field and that the signal drops significantly when the angular frequency  $\omega$  of the oscillating magnetic field is much larger than  $\Gamma$ .

**Discussion of magnetometer sensitivity.** The sensitivity of our magnetometer is around  $120 \text{ fT}/\sqrt{\text{Hz}}$  for frequencies in the 100–500 Hz range, and around or better than  $300 \text{ fT}/\sqrt{\text{Hz}}$  for frequencies in the wider range 5–1000 Hz [see Fig. 3(d)]. Improving the sensitivity will be beneficial for biomedical experiments. Our current magnetometer is based on free-space laser beams with  $\approx 1 \text{ m}$  propagation distances, and for that reason the setup is quite sensitive to vibrations and air-flows. A more compact magnetometer is expected to be crucial for improving the sensitivity. 50 Hz noise and possibly low-frequency (DC–200 Hz) magnetic field noise are also problematic. Active stabilization of the background magnetic field would improve those noise sources. The sensitivity is ultimately limited by the quantum spin-projection noise of the cesium atoms<sup>15</sup> which at room-temperature is estimated to be  $1/(\gamma\sqrt{T_2 2nV}) = 8 \text{ fT}/\sqrt{\text{Hz}}$  using the density of atoms  $n = 3.0 \cdot 10^{16} \text{ m}^{-3}$  (for  $T \approx 20^\circ\text{C}$ ), sensing volume  $V = (5 \text{ mm})^3$  and  $T_2 = 4 \text{ ms}$ . At human-body temperature  $37^\circ\text{C}$ , the density of atoms is four times higher leading to a quantum-limited sensitivity of  $4 \text{ fT}/\sqrt{\text{Hz}}$ . Our type of magnetometer has previously achieved sub-femtotesla sensitivity mainly limited by quantum noise for detection of radio-frequency magnetic fields<sup>14</sup>.

**Isolated guinea pig heart preparations.** The experiments were approved by the Danish Veterinary and Food Administration, Ministry of Environment and Food of Denmark under License No. 2014-15-2934-01061 and were carried out in accordance with the European Community Guidelines for the Care and Use of Experimental Animals. The experiments were performed using female Dunkin Hartley guinea pigs (300–450 g, Charles River, Saint-Germain-Nuelle, France). Guinea pigs were anesthetized with an intraperitoneal injection of pentobarbital 200 mg/ml and lidocaine hydrochloride 20 mg/ml (Glostrup Apotek, Denmark), dose 0.150 ml/100 g BW. A tracheostomy was performed and the guinea pigs were ventilated (3.5 ml/60 strokes/min) through a rodent ventilator (7025 Rodent ventilator, Ugo Basile, Italy). The hearts were cannulated *in situ* through an incision of the aorta and connected to the Langendorff retrograde perfusion set-up (Hugo Sachs Elektronik, Harvard Apparatus GmbH, March, Germany). The hearts were retrogradely perfused at a constant perfusion pressure of 60 mmHg with a  $5^\circ\text{C}$ , pH 7.8, cardioplegia buffer (in mM: NaCl 110,  $\text{NaHCO}_3$  25, KCl 16,  $\text{CaCl}_2$  1.2,  $\text{MgCl}_2$  16). At cardiac arrest the hearts were submerged in  $5^\circ\text{C}$  cardioplegia buffer and transported to a different laboratory where the magnetometer was located. Here, the hearts were revived by a retrogradely perfusion of  $37^\circ\text{C}$  Krebs-Henseleit buffer (in mM: NaCl 120,  $\text{NaHCO}_3$  25,  $\text{KCl}$ ,  $\text{MgSO}_4$  0.6,  $\text{NaH}_2\text{PO}_4$  0.6,  $\text{CaCl}_2$  2.5, Glucose 11) saturated with 95%  $\text{O}_2$  and 5%  $\text{CO}_2$ . The hearts were continuously perfused with a coronary flow ranging from 9–14 ml/min. The spontaneously beating hearts were mounted in a custom made watertight acrylic container (inner size 35 mm, wall thickness 2 mm) during the following measurements. The aortic perfusion pressure was determined with an ISOTEC transducer (Hugo Sachs Elektronik), and the coronary flow was measured with an ultrasonic flowmeter (Transonic Systems INC, USA). Both were connected to an amplifier (Hugo Sachs Elektronik). Perfusion pressure and coronary flow signals were sampled at a frequency of 2 kHz and converted by a 16/30 data acquisition system from PowerLab systems (ADInstruments, Oxford, UK) and monitored by using LabChart 7 software (ADInstruments).

**Pharmacology.** The hearts were perfused with  $0.06 \mu\text{M}$  E-4031 (Sigma-Aldrich, Darmstadt, Germany), a class III anti-arrhythmic drug, that blocks the repolarizing  $\text{I}_{Kr}/\text{hERG}/\text{K}_v$  11.1 current, and thereby prolong the ventricular action potential demonstrated by prolonged QT-intervals.

**Size of guinea-pig hearts.** Six isolated guinea-pig hearts were used for the measurements presented here. The size of the hearts are given in Supplementary Table S1. The mean biventricular diameter was 16.8 mm and the mean length was 23.3 mm. The size of the hearts are similar to that of a human fetus at gestational age of 18–22 weeks<sup>34</sup>.

## Data Availability

The datasets generated during and/or analysed during the current study are available from the corresponding author on reasonable request.

## References

- Wacker-Gusmann, A., Strasburger, J. F., Cuneo, B. F. & Wakai, R. T. Diagnosis and treatment of fetal arrhythmia. *Am J Perinatol.* **31**, 617–628 (2014).
- Baule, G. & McFee, R. Detection of the magnetic field of the heart. *American Heart Journal* **66**, 95–96 (1963).
- Cohen, D., Edelsack, E. A. & Zimmerman, J. E. Magnetocardiograms taken inside a shielded room with a superconducting point contact magnetometer. *Appl. Phys. Lett.* **16**, 278–280 (1970).
- Xia, H., Ben-Amar Baranga, A., Hoffman, D. & Romalis, M. V. Magnetoencephalography with an atomic magnetometer. *Appl. Phys. Lett.* **89**, 211104 (2006).
- Boto, E. *et al.* A new generation of magnetoencephalography: Room temperature measurements using optically-pumped magnetometers. *NeuroImage* **149**, 404–414 (2017).
- Boto, E. *et al.* Moving magnetoencephalography towards real-world applications with a wearable system. *Nature* **555**, 657–661 (2018).
- Bison, G. *et al.* A room temperature 19-channel magnetic field mapping device for cardiac signals. *Appl. Phys. Lett.* **95**, 173701 (2009).
- Lembke, G. *et al.* Optical multichannel room temperature magnetic field imaging system for clinical application. *Biomed. Opt. Express* **5**, 876–881 (2014).
- Wyllie, R., Kauer, M., Wakai, R. T. & Walker, T. G. Optical magnetometer array for fetal magnetocardiography. *Opt. Lett.* **37**, 2247–2249 (2012).

10. Alem, O. *et al.* Fetal magnetocardiography measurements with an array of microfabricated optically pumped magnetometers. *Phys. Med. Biol.* **60**, 4797 (2015).
11. Eswaran, H., Escalona-Vargas, D., Bolin, E. H., Wilson, J. D. & Lowery, C. L. Fetal magnetocardiography using optically pumped magnetometers: a more adaptable and less expensive alternative? *Prenatal Diagnosis* **37**, 193–196 (2017).
12. Kominis, I. K., Kornack, T. W., Allred, J. C. & Romalis, M. V. A subfemtotesla multichannel atomic magnetometer. *Nature* **422**, 596–599 (2003).
13. [www.quspin.com](http://www.quspin.com). (Accessed: 22nd July 2018).
14. Wasilewski, W. *et al.* Quantum noise limited and entanglement-assisted magnetometry. *Phys. Rev. Lett.* **104**, 133601 (2010).
15. Jensen, K. *et al.* Non-invasive detection of animal nerve impulses with an atomic magnetometer operating near quantum limited sensitivity. *Scientific Reports* **6**, 29638 (2016).
16. Morales, S. *et al.* Magnetocardiography measurements with  $^4\text{He}$  vector optically pumped magnetometers at room temperature. *Phys. Med. Biol.* **62**, 7267 (2017).
17. Simpson, J. M. Impact of fetal echocardiography. *Ann Pediatr Card* **2**, 41–50 (2009).
18. Leeuwen, P. *et al.* Magnetocardiography in the diagnosis of fetal arrhythmia. *Br J Obstet Gynaecol.* **106**, 1200–1208 (1999).
19. Zhao, H. *et al.* Electrophysiological characteristics of fetal atrioventricular block. *J Am Coll Cardiol.* **51**, 77–84 (2008).
20. Wakai, R., Strasburger, J., Li, Z., Deal, B. & Gotteiner, N. Magnetocardiographic rhythm patterns at initiation and termination of fetal supraventricular tachycardia. *Circulation* **107**, 307–312 (2003).
21. Cuneo, B. F. *et al.* In utero diagnosis of long QT syndrome by magnetocardiography. *Circulation* **128**, 2183–2191 (2013).
22. Cuneo, B. F., Strasburger, J. F. & Wakai, R. T. The natural history of fetal long QT syndrome. *J Electrocardiol.* **49**, 807 (2016).
23. Schwartz, P. J. *et al.* Prevalence of the congenital long-QT syndrome. *Circulation* **120**, 1761–1767 (2009).
24. Lieve, K. V. V. & Wilde, A. A. M. Inherited ion channel diseases: a brief review. *EP Europace* **17**, ii1–ii6 (2015).
25. Cuneo, B. F. & Strasburger, J. F. We only find what we look for: fetal heart rate and the diagnosis of long-QT syndrome. *Circulation. Arrhythmia and electrophysiology* **8**, 760–762 (2015).
26. von Steinburg, P. *et al.* What is the normal fetal heart rate? *PeerJ* **1**, e82 (2013).
27. American College of Obstetricians and Gynecologists. ACOG Practice Bulletin No. 106: Intrapartum fetal heart rate monitoring: nomenclature, interpretation, and general management principles. *Obstetrics & Gynecology* **114**, 192 (2009).
28. Farraj, A. K., Hazari, M. S. & Cascio, W. E. The utility of the small rodent electrocardiogram in toxicology. *Toxicological Sciences* **121**, 11–30 (2011).
29. Bell, R. M., Mocanu, M. M. & Yellon, D. M. Retrograde heart perfusion: The Langendorff technique of isolated heart perfusion. *Journal of Molecular and Cellular Cardiology* **50**, 940–950 (2011).
30. Ledbetter, M. P., Savukov, I. M., Acosta, V. M., Budker, D. & Romalis, M. V. Spin-exchange-relaxation-free magnetometry with Cs vapor. *Phys. Rev. A* **77**, 033408 (2008).
31. Borna, A. *et al.* A 20-channel magnetoencephalography system based on optically pumped magnetometers. *Phys. Med. Biol.* **62**, 8909 (2017).
32. Alem, O. *et al.* Magnetic field imaging with microfabricated optically-pumped magnetometers. *Opt. Express* **25**, 7849–7858 (2017).
33. Marmugi, L. & Renzoni, F. Optical magnetic induction tomography of the heart. *Scientific Reports* **6**, 23962 (2016).
34. Li, X., Zhou, Q., Huang, H., Tian, X. & Peng, Q. Z-score reference ranges for normal fetal heart sizes throughout pregnancy derived from fetal echocardiography. *Prenatal Diagnosis* **35**, 117–124 (2015).
35. Hamlin, R. L., Kijitawornrat, A., Keene, B. W. & Hamlin, D. M. QT and RR Intervals in Conscious and Anesthetized Guinea Pigs with Highly Varying RR Intervals and Given QTc-Lengthening Test Articles. *Toxicological Sciences* **76**, 437–442 (2003).

## Acknowledgements

This work was supported by the Danish Quantum Innovation Center (QUBIZ)/Innovation Fund Denmark, the ERC Proof of Concept grant QUMAG, the ERC AdG QUANTUM-N, and the U. S. Army Research Laboratory and the U. S. Army Research Office under contract/grant number Grant No. W911NF-11-0235.

## Author Contributions

K.J., M.A.S., H.S., J.A., B.H.B. performed the experiments. M.A.S. and B.H.B. prepared the animal hearts. M.V.B. designed and fabricated the vapor cell. K.J., M.A.S. and B.H.B. wrote the manuscript. All authors discussed the results and commented on the manuscript. B.H.B., S.-P.O. and E.S.P. supervised the research.

## Additional Information

**Supplementary information** accompanies this paper at <https://doi.org/10.1038/s41598-018-34535-z>.

**Competing Interests:** The authors declare no competing interests.

**Publisher's note:** Springer Nature remains neutral with regard to jurisdictional claims in published maps and institutional affiliations.



**Open Access** This article is licensed under a Creative Commons Attribution 4.0 International License, which permits use, sharing, adaptation, distribution and reproduction in any medium or format, as long as you give appropriate credit to the original author(s) and the source, provide a link to the Creative Commons license, and indicate if changes were made. The images or other third party material in this article are included in the article's Creative Commons license, unless indicated otherwise in a credit line to the material. If material is not included in the article's Creative Commons license and your intended use is not permitted by statutory regulation or exceeds the permitted use, you will need to obtain permission directly from the copyright holder. To view a copy of this license, visit <http://creativecommons.org/licenses/by/4.0/>.

© The Author(s) 2018